Comput. Methods Appl. Mech. Engrg. 197 (2008) 4353–4366

Contents lists available at ScienceDirect

Comput. Methods Appl. Mech. Engrg.

journal homepage: www.elsevier.com/locate/cma

Stabilized low-order finite elements for coupled solid-deformation/fluid-diffusion and their application to fault zone transients

Joshua A. White, Ronaldo I. Borja *

Department of Civil and Environmental Engineering, Stanford University, Stanford, CA 94305, USA

ARTICLE INFO

Article history:
Received 29 December 2007
Received in revised form 5 May 2008
Accepted 7 May 2008
Available online 7 July 2008

Keywords:
Coupled analysis
Fault zone
Fluid flow
Mixed formulation
Stabilized finite elements

ABSTRACT

Finite element simulations of coupled solid-deformation/fluid-diffusion occurring in earthquake fault zones often require high-fidelity descriptions of the spatial and temporal variations of excess pore water pressure. Large-scale calculation of the coupled fault zone process is often inhibited by the high-order interpolation of the displacement field required to overcome unstable tendencies of the finite elements in the incompressible and nearly incompressible limit. In this work we utilize a stabilized formulation in which the balance of mass is augmented with an additional term representing a stabilization to the incremental change in the pressure field. The stabilized formulation permits equal-order interpolation for the displacement and pore pressure fields and suppresses pore pressure oscillations in the incompressible and nearly incompressible limit. The technique is implemented with a recently developed critical state plasticity model to investigate transient fluid-flow/solid-deformation processes arising from slip weakening of a fault segment. The accompanying transient pore pressure development and dissipation can be used to predict fault rupture and directivity where fluid flow is an important driving force.

© 2008 Elsevier B.V. All rights reserved.

1. Introduction

In order to accurately model the behavior of fluid-saturated geomaterials, it is necessary to account for the strong coupling between the solid skeleton and pore fluid. This coupling is of particular interest when studying fault zone processes, and is central to many open questions about fault behavior. The presence of fluids might explain why some faults, such as the San Andreas, are weaker than expected [1,2]. Increases in pore pressure may tend to weaken faults by reducing the effective normal stress, and trigger seismic activity. If the overpressures are too large, however, the fault could experience stable, rather than unstable, sliding [3]. Dilatancy or compaction within the fault zone will also play a crucial role, as well as the degree to which fluid exchange is allowed to occur between the fault and its surroundings.

Finite element simulations provide a natural tool for investigating these processes. To do so, we employ a mixed $\boldsymbol{u}/p$ formulation to solve for the solid displacements and fluid pressures. In comparison to pure-displacement formulations, however, the mixed scheme creates additional challenges for the numerical analyst. In the limit of low permeability or fast loading rates, the pore fluid can impose near or exact incompressibility on the deformation of the solid matrix. In the presence of incompressibility constraints, it is well known that only certain combinations of discrete spaces for the pressure and displacement interpolation exhibit stable behavior. Failure to choose a stable pair can lead to poor results, typically in the form of spurious oscillations in the pressure field and sub-optimal convergence behavior.

The same restrictions are found in other constrained problems in solid and fluid mechanics. Classic examples include mixed formulations for Stokes flow, Darcy flow, and incompressible elasticity. The mathematical theory establishing the solvability and stability characteristics of mixed formulations is well-developed. The key ingredients are the ellipticity requirement and the famous Ladyzhenskaya-Babuška-Brezzi (LBB) condition [4,5]. Unfortunately, many seemingly natural interpolation pairs – including equal-order interpolation for all field variables – do not satisfy the necessary stability requirements. In practice, most analysts rely on "safe" elements such as the Taylor-Hood family, in which the displacement interpolation is one-order higher than the pressure interpolation. A variety of more sophisticated stable elements are also available, for example, [6,7].

From an implementation point of view, it would be appealing to circumvent the stability restrictions and employ a broader class of interpolation pairs. Over the years, many stabilization techniques have been proposed for doing precisely this, most extensively in the fluid dynamics community. The model equations used to study these schemes are typically the Stokes or Darcy equations, which despite their simplicity contain all of the salient features of a constrained problem. We mention the early Brezzi-Pitkäranta scheme [8], the Galerkin Least-Squares (GLS) approach of Hughes et al., [9],

* Corresponding author.
E-mail address: borja@stanford.edu (R.I. Borja).

0045-7825/$ - see front matter © 2008 Elsevier B.V. All rights reserved.
doi:10.1016/j.cma.2008.05.015

and the more recent Variational Multiscale Methods [10] – but many others exist [11–13]. In solid mechanics, a variety of schemes have also been developed for incompressible and quasi-incompressible elasticity in order to overcome volumetric locking associated with pure-displacement formulations. For example, Oñate et al. [14] proposed a formulation based on the concept of Finite Calculus. Masud and Xia [15,16] developed a formulation for both linear and nonlinear constitutive models based on a Variational Multiscale approach. Romero and Bischoff have recently proposed an interesting method for linear elasticity which involves enriching the finite element spaces with incompatible bubble functions [17]. Of course, the above schemes are merely a representative sample of an extensive literature that has developed for each class of problems.

While it is difficult to classify all stabilization schemes in a unified framework, most frequently the methods lead to a modified variational formulation in which additional terms are added to the mass balance equation, modifying the incompressibility constraint in such a way that stability of the mixed formulation is increased while maintaining a convergent method. In this way, meaningful results can be obtained when using otherwise unstable elements. The goal of this contribution is to extend the stabilization concept to coupled solid-deformation/fluid-diffusion problems. While stabilized methods are employed frequently in fluid and solid mechanics problems, their use in coupled geomechanical problems is limited. Nevertheless, some good work in this direction has begun. In [18], Wan used the GLS approach to stabilize both a displacement–pressure and a displacement–pressure–velocity formulation. In [19,20], Truty and Zimmerman compared three schemes: one based on the Brezzi-Pitkäranta stabilization and two based on the GLS approach. They also extended their formulation to account for partial saturations. In [21,22], Pastor et al. proposed a stabilization scheme for dynamic problems using a fractional-step algorithm, incorporating the stabilization into the time-stepping scheme. In each case, the authors demonstrated that the stabilizations can successfully suppress instabilities and lead to good-quality solutions. Of course, each scheme has its own shortcomings. For example, the GLS method is based on adding the residual of the strong form of the governing equations. As such, second-order derivatives with respect to the displacements appear, and when using linear interpolation, these terms either vanish or are poorly approximated. A special technique must generally be employed to improve the accuracy of these calculations, introducing additional computational work. See [18], for example, where Wan develops such a stress recovery technique. The GLS formulations also often lead to a non-symmetric modification of the system matrix. While this makes little difference if the original problem is non-symmetric, it would be appealing to preserve any symmetry if it does exist. Indeed, a key advantage of the methods of [15–17] is their symmetry-preserving property, but these schemes have only been employed for incompressible solids and have not been extended to coupled solid/fluid formulations. The Brezzi-Pitkäranta scheme does lead to a symmetric modification and can be cheaply implemented for equal-order linear interpolations. Unfortunately, the formulation cannot be extended to stabilize other unstable pairs such as linear-displacement/constant-pressure elements. The fractional-step method is primarily designed for dynamic problems, and may not be an efficient approach for quasi-static models. It also leads to a conditionally stable time-integration scheme even if the underlying algorithm is implicit, though recent improvements by the authors have significantly improved the stability restriction [23].

In this paper, we introduce a new stabilization scheme for coupled geomechanical problems based on the concept of Polynomial-Pressure-Projections. In this approach, the additional stabilizing terms use element-local projections of the pressure field to counteract the inherent instabilities in the chosen interpolation pair. The technique was recently proposed by Dohrmann, Bochev, and Gunzburger, and has been successfully employed for stabilizing the Stokes problem [13,24] and Darcy problem [25]. An analysis of similar pressure projection methods, and a unifying framework for their analysis, has also been proposed by Burman [26].

In this work we employ pressure projections to address instabilities that arise in the geomechanical problems under consideration. The new stabilization has several appealing features. In particular, the additional stabilizing terms can be assembled locally on each element using standard shape function information, and no specialized subroutines are required. The scheme does not require the calculation of higher-order derivatives or special stress-recovery techniques. The method introduces minimal additional computational work, and can be readily implemented in a standard finite element code. The scheme also leads to a symmetric modification of the system matrix, preserving any symmetry that was inherent in the original variational formulation. The resulting method thus shares many of the positive features of the Brezzi-Pitkäranta stabilization, but can be used to stabilized a broader class of unstable pairs.

The primary motivation for using stabilization is computational efficiency. As an example, consider two meshes composed of an equal number of elements. The first mesh employs continuous biquadratic-displacement/bilinear-pressure quads (Q9P4), while the second uses bilinear-displacement/bilinear-pressure quads (Q4P4). Both elements are illustrated in Fig. 1. The first element possesses 22 degrees of freedom and is known to be stable, while the second element has 12 degrees of freedom and is known to be unstable – unless a stabilized formulation is employed. The two elements are comparable in the sense that they produce the same order of pressure interpolation. The Q9P4, however, leads to algebraic problems with many more degrees of freedom. As the number of elements in each mesh grows, a simple argument shows that the total number of unknowns in the two meshes quickly approaches a ratio of 3:1. If we consider the equivalent three-dimensional situation, this ratio approaches $6\frac{1}{4}:1$. The bandwidth of the sparsity patterns will grow similarly.

Further computational savings can also be associated with the quadrature rule employed. The Q9P4 element typically requires 3×3 Gauss-quadrature in order to accurately integrate the quadratic displacement field. In the Q4P4 mesh, we only need 2×2 quadrature. If we consider an elastoplastic material in which a significant level of computation must be performed in the material subroutine at each Gauss point, the lower-order quadrature rule will lead to additional efficiency. The equal-order element can also somewhat simplify the code implementation, particularly when employing adaptive mesh refinement or a parallel decomposition of the domain. Finally we note that the introduction of stabilization terms can often improve the convergence behavior of iterative solvers. For extremely large problems, the memory-efficiency of iterative solvers makes them a more attractive choice than sparse direct solvers. For an extensive discussion of the numerical solution of algebraic systems of the type considered here, see [27].

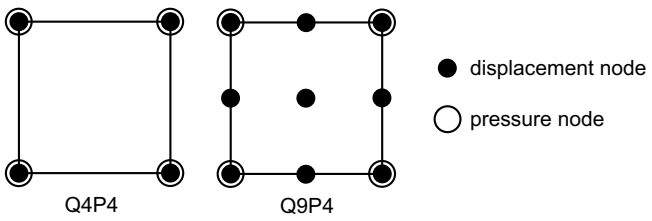

Fig. 1. Example mixed elements, showing the unstable Q4P4 and stable Q9P4.

Stabilized low-order finite elements are very useful for improving the spatial and temporal resolution of excess pore pressure in large-scale fault-slip simulations. In this paper we demonstrate how the proposed stabilization scheme can be used to couple fluid diffusion phenomena with fault weakening mechanisms. We employ classical plasticity theory along with critical state soil mechanics to represent the solid deformation behavior. The yield surface is an ellipsoid that grows with plastic volumetric compaction; an associative flow rule is used to characterize the plastic flow. The compression cap of the yield surface is responsible for generating excess pore pressure due to shear-induced compaction as the fault slips. In addition, fault activation is known to trigger slip weakening mechanisms [28–30], including a reduction in the effective friction angle of the fault gouge material [31], thus further enhancing the development of excess pore pressure. All of these processes are intimately linked and modeled simultaneously in a numerical example demonstrating the efficacy of the stabilized formulation.

The rest of the paper is organized as follows. First, we present the governing equations and finite element implementation of a quasi-static $\boldsymbol{u}/p$ formulation. The formulation includes material nonlinearity in the form of a critical state plasticity model in a small deformation format. Next, we modify the scheme to include new stabilization terms, focusing on stabilizing the equal-order Q4P4 element. We then demonstrate the performance of the new scheme on several numerical examples. Two examples are taken from familiar geotechnical applications. The first has an analytical solution, while the second's qualitative behavior is well-understood. The final example is devoted to modeling the transient pore-pressure behavior around an idealized fault zone. The examples cover a wide range of material models: linear-elastic, hyperelastic, and elastoplastic. In all cases we compare the performance of a reference stable element (Q9P4), an unstable element (Q4P4), and the same unstable element with stabilization (denoted Q4P4s). For completeness, we also attempt to highlight certain situations where the stabilization scheme must be employed with caution.

2. Coupled formulation

In this section we present a coupled formulation for fluid-saturated geomaterials. We include material nonlinearity in the description, but exclude any geometric effects due to large deformations. Our starting point is the strong and weak forms of the governing equations, as well as material models for the solid and fluid constituents. We then describe spatial and temporal discretizations, leading to a system of nonlinear equations. We also discuss the linearization of this system and its iterative solution using Newton's method.

2.1. Governing equations

In this work, we consider a two-phase mixture consisting of a solid matrix and saturating fluid. We assume that the solid and fluid constituents can both be modeled as incompressible, and that the system remains isothermal. In this case, we may write the local forms of the balance of linear momentum and balance of mass as [32,33]

$$\nabla \cdot (\boldsymbol{\sigma}' - p\mathbf{1}) + \rho \boldsymbol{g} = \mathbf{0} \quad \text{(Equilibrium)}, \tag{1a}$$

$$\nabla \cdot \dot{\boldsymbol{u}} + \nabla \cdot \tilde{\boldsymbol{v}} = 0 \quad \text{(Continuity)}. \tag{1b}$$

Here, $\boldsymbol{\sigma}'$ = effective Cauchy stress tensor, p = excess pore pressure (i.e. pressure in excess of that at steady state), $\mathbf{1}$ = second-order unit tensor, $\boldsymbol{u}$ = displacement field for the solid matrix, $\tilde{\boldsymbol{v}}$ = superficial velocity field (average relative velocity of seepage per unit total area), ρ = buoyant density of the mixture in the saturating fluid, and $\boldsymbol{g}$ = vector of gravity accelerations. It is also common to see the balance equations expressed in terms of the total pressure rather than the excess pressure. The major difference lies in the definition of the constitutive equation for the fluid, which either relates the superficial velocity to the excess or the total pressure. In the current case we employ a generalized Darcy law of the form

$$\tilde{\boldsymbol{v}} = -\frac{1}{\rho_f g}\boldsymbol{k} \cdot \nabla p, \tag{2}$$

where $\boldsymbol{k}$ =tensor of hydraulic conductivities (with typical units of m/s), ρ_f =density of the fluid phase, and $g = \|\boldsymbol{g}\|$. We emphasize that one should use the buoyant density of the mixture, rather than the total density, when employing an excess pressure formulation.

We must also introduce a constitutive equation for the effective stress, which for now we express in general rate form

$$\dot{\boldsymbol{\sigma}}' = \mathbb{C}^{ep} : \dot{\boldsymbol{\epsilon}}; \qquad \boldsymbol{\epsilon} = \nabla^s \boldsymbol{u} = \frac{1}{2}\left(\nabla \boldsymbol{u} + \nabla \boldsymbol{u}^{\mathrm{T}}\right). \tag{3}$$

Here, $\mathbb{C}^{ep}$ = fourth-order tensor of tangential moduli. In the following derivations we assume we have a nonlinear material model that can be expressed in form (3). A complete description of the critical state plasticity model employed will be given in Section 4.

The mixture occupies a domain Ω with boundary Γ. This boundary is suitably decomposed into regions where essential and natural boundary conditions are specified for both the solid and fluid. In particular, we define:

- Γ_u: solid displacement boundary.
- Γ_t: solid traction boundary.
- Γ_p: fluid pressure boundary.
- Γ_q: fluid flux boundary.

This decomposition is subject to the restrictions

$$\Gamma = \Gamma_u \cup \Gamma_t = \Gamma_p \cup \Gamma_q, \tag{4}$$

$$\Gamma_u \cap \Gamma_t = \Gamma_p \cap \Gamma_q = \varnothing. \tag{5}$$

The boundary conditions are given as

$$\boldsymbol{u} = \overline{\boldsymbol{u}} \quad \text{on } \Gamma_u \quad \text{(specified displacement)}, \tag{6}$$

$$\boldsymbol{n} \cdot \boldsymbol{\sigma}' = \overline{\boldsymbol{t}} \quad \text{on } \Gamma_t \quad \text{(specified traction)}, \tag{7}$$

$$p = \overline{p} \quad \text{on } \Gamma_p \quad \text{(specified pressure)}, \tag{8}$$

$$-\boldsymbol{n} \cdot \tilde{\boldsymbol{v}} = \overline{q} \quad \text{on } \Gamma_q \quad \text{(specified flux)}. \tag{9}$$

Finally, initial conditions at $t = 0$ are given as $\{\boldsymbol{u}_0, p_0\}$.

2.2. Variational form

For the purposes of the finite element implementation, we present the weak form of the boundary value problem. First, two spaces of trial functions are defined as

$$S_u = \{\boldsymbol{u} : \Omega \to \mathbb{R}^3 | \boldsymbol{u} \in \boldsymbol{H}^1, \boldsymbol{u} = \overline{\boldsymbol{u}} \quad \text{on } \Gamma_u\}, \tag{10}$$

$$S_p = \{p : \Omega \to \mathbb{R} | p \in H^1, p = \overline{p} \quad \text{on } \Gamma_p\}, \tag{11}$$

where H^1 denotes a Sobolev space of degree one. We also define the corresponding spaces of weighting functions, with homogeneous conditions on the essential boundaries,

$$V_u = \{\boldsymbol{\eta} : \Omega \to \mathbb{R}^3 | \boldsymbol{\eta} \in \boldsymbol{H}^1, \boldsymbol{\eta} = \mathbf{0} \text{ on } \Gamma_u\}, \tag{12}$$

$$V_p = \{\psi : \Omega \to \mathbb{R} | \psi \in H^1, \psi = 0 \text{ on } \Gamma_p\}. \tag{13}$$

The weak form of the problem is then to find $\{\boldsymbol{u}, p\} \in S_u \times S_p$ such that for all $\{\boldsymbol{\eta}, \psi\} \in V_u \times V_p$,

$$\mathscr{G} = \int_\Omega (\nabla^s \boldsymbol{\eta} : \boldsymbol{\sigma}' - p\nabla\cdot\boldsymbol{\eta} - \boldsymbol{\eta}\cdot\rho\mathbf{g})\mathrm{d}\Omega - \int_{\Gamma_t} \boldsymbol{\eta}\cdot\bar{\mathbf{t}}\,\mathrm{d}\Gamma = 0 \quad \text{(Equilibrium)}, \tag{14a}$$

$$\mathscr{H} = \int_\Omega (-\psi\nabla\cdot\dot{\boldsymbol{u}} + \nabla\psi\cdot\tilde{\boldsymbol{v}})\mathrm{d}\Omega + \int_{\Gamma_q} \psi\bar{q}\,\mathrm{d}\Gamma = 0 \quad \text{(Continuity)}. \tag{14b}$$

It is useful to compare the above mixed formulation with those encountered for other incompressible problems in solid and fluid mechanics – especially in the definition of the spaces S_p and V_p. In mixed formulations for incompressible elasticity or Stokes' flow, the pressures are usually only required to be in L_2 (or perhaps $L_2/\mathbb{R}$) and no essential boundary conditions are specified. The case is somewhat different when we consider a fluid saturated porous medium with non-zero permeability. At the initial moment of loading, as $t \to 0$ and no time has passed for drainage to occur, the medium acts as an incompressible solid, with the pore pressures serving as Lagrange multipliers to enforce the incompressibility constraint. As time passes and drainage proceeds, however, the fundamental character of the fluid flow problem switches to a diffusion equation, with the pore-pressure becoming a potential determining the velocity field. It is for this reason that it is appropriate to require the pressures be in H^1 and specify essential boundary conditions on them. The diffusive nature of the pressures distinguishes the current problem from comparable incompressible problems encountered in other fields. An interesting discussion of these considerations can be found in Murad and Loula [34], where the authors consider the variational form of the linear Biot consolidation equations as three separate problems: one governing the system at the moment of loading, another describing the time-dependent deformation/diffusion process, and another describing the steady-state system when all excess pressures have dissipated.

2.3. Discretization in time

Given the time-dependent nature of the variational form, we introduce a temporal discretization using a generalized trapezoidal integration method [35]. We rewrite the balance of mass at a discrete time step n such that

$$\mathscr{H}_{n+1} = \int_\Omega \left(-\psi\nabla\cdot\frac{\boldsymbol{u}_{n+1}-\boldsymbol{u}_n}{\Delta t} + \nabla\psi\cdot\tilde{\boldsymbol{v}}_{n+\theta}\right)\mathrm{d}\Omega + \int_{\Gamma_q}\psi\bar{q}_{n+\theta}\mathrm{d}\Gamma = 0, \tag{15}$$

where

$$\bar{q}_{n+\theta} = \theta\bar{q}_{n+1} + (1-\theta)\bar{q}_n, \tag{16}$$

$$\tilde{\boldsymbol{v}}_{n+\theta} = \theta\tilde{\boldsymbol{v}}_{n+1} + (1-\theta)\tilde{\boldsymbol{v}}_n, \tag{17}$$

and $\theta \in [0,1]$ is an integration parameter. Common choices include $\theta = 1$, giving the first-order accurate backward-Euler scheme, and $\theta = 1/2$, giving the second-order accurate Crank-Nicolson scheme. The equilibrium equation $\mathscr{G}$ does not contain any time-derivatives, and we implicitly evaluate all terms at step $n+1$.

2.4. Linearization

In general, $\mathscr{G}$ and $\mathscr{H}$ (or the time-discrete versions $\mathscr{G}_{n+1}$ and $\mathscr{H}_{n+1}$) represent two nonlinear residual equations that must be solved using an iterative procedure. To do so, we implement a Newton–Raphson scheme, in which we expand the governing equations about a trial configuration $(\boldsymbol{u}_k, p_k)$ using a linear model, i.e.

$$0 = \mathscr{G}(\boldsymbol{u},p,\boldsymbol{\eta}) \approx \mathscr{G}(\boldsymbol{u}_k,p_k,\boldsymbol{\eta}) + \Delta\mathscr{G}(\Delta\boldsymbol{u}_k,\Delta p_k,\boldsymbol{\eta}), \tag{18}$$

$$0 = \mathscr{H}(\boldsymbol{u},p,\psi) \approx \mathscr{H}(\boldsymbol{u}_k,p_k,\psi) + \Delta\mathscr{H}(\Delta\boldsymbol{u}_k,\Delta p_k,\psi), \tag{19}$$

which leads to an iterative update scheme in which we solve,

$$\Delta\mathscr{G}(\Delta\boldsymbol{u}_k,\Delta p_k,\boldsymbol{\eta}) = -\mathscr{G}(\boldsymbol{u}_k,p_k,\boldsymbol{\eta}), \tag{20}$$

$$\Delta\mathscr{H}(\Delta\boldsymbol{u}_k,\Delta p_k,\psi) = -\mathscr{H}(\boldsymbol{u}_k,p_k,\psi), \tag{21}$$

for the incremental variations $\Delta\boldsymbol{u}_k$ and Δp_k, and update $\boldsymbol{u}_{k+1} = \boldsymbol{u}_k + \Delta\boldsymbol{u}_k$ and $p_{k+1} = p_k + \Delta p_k$. Thus within each time-step (with index n) we solve a sequence of linear problems (with index k) to find the configuration satisfying the residual equations. Upon convergence, $n \leftarrow (n+1)$ and $k \leftarrow 0$.

For the equilibrium equation,

$$\Delta\mathscr{G}_k = \int_\Omega (\nabla^s\boldsymbol{\eta} : \mathbb{C}_k : \nabla^s\Delta\boldsymbol{u}_k - \Delta p_k\nabla\cdot\boldsymbol{\eta})\mathrm{d}\Omega, \tag{22}$$

where

$$\mathbb{C}_k \equiv \frac{\partial\boldsymbol{\sigma}'_k}{\partial\boldsymbol{\epsilon}_k} \tag{23}$$

is the fourth-order tensor of algorithmic tangent moduli. For the continuity equation,

$$\Delta\mathscr{H}_k = \int_\Omega \left(-\psi\nabla\cdot\frac{\Delta\boldsymbol{u}_k}{\Delta t} - \theta\nabla\psi\cdot\frac{\boldsymbol{k}}{\rho_f g}\cdot\nabla\Delta p_k\right)\mathrm{d}\Omega. \tag{24}$$

2.5. Discretization in space

We now consider an element partitioning of the domain Ω. In the standard manner, we introduce a discrete trial space $S_u^h \times S_p^h$ and weighting space $V_u^h \times V_p^h$ corresponding to the chosen finite element interpolations. We use a superscript h to indicate spatially-discrete quantities, just as we use subscripts n and $n+1$ to indicate temporally-discrete quantities. The fully discrete variational statement of the problem is now: find $\{\boldsymbol{u}^h_{n+1}, p^h_{n+1}\} \in S_u^h \times S_p^h$ such that for all $\{\boldsymbol{\eta}^h, \psi^h\} \in V_u^h \times V_p^h$,

$$\mathscr{G}^h_{n+1} = \int_\Omega (\nabla^s\boldsymbol{\eta}^h : \boldsymbol{\sigma}'_{n+1} - p^h_{n+1}\nabla\cdot\boldsymbol{\eta}^h - \boldsymbol{\eta}^h\cdot\rho\mathbf{g})\mathrm{d}\Omega - \int_{\Gamma_t}\boldsymbol{\eta}^h\cdot\bar{\mathbf{t}}_{n+1}\mathrm{d}\Gamma = 0, \tag{25a}$$

$$\mathscr{H}^h_{n+1} = \int_\Omega \left(-\psi^h\nabla\cdot\frac{\boldsymbol{u}^h_{n+1}-\boldsymbol{u}^h_n}{\Delta t} + \nabla\psi^h\cdot\tilde{\boldsymbol{v}}^h_{n+\theta}\right)\mathrm{d}\Omega + \int_{\Gamma_q}\psi^h\bar{q}_{n+\theta}\mathrm{d}\Gamma = 0. \tag{25b}$$

The displacement and pore pressure fields are approximated as

$$\boldsymbol{u}^h = \boldsymbol{N}^d\boldsymbol{d}, \quad p^h = \boldsymbol{N}^p\boldsymbol{p}, \tag{26}$$

where $\boldsymbol{N}^d$ and $\boldsymbol{N}^p$ are arrays of displacement and pressure shape functions, and $\boldsymbol{d}$ and $\boldsymbol{p}$ are corresponding vectors of unknowns. The weighting functions are represented as

$$\boldsymbol{\eta}^h = \boldsymbol{N}^d\boldsymbol{c}, \quad \psi^h = \boldsymbol{N}^p\bar{\boldsymbol{c}}. \tag{27}$$

Further, we define the following transformation matrices:

$$\nabla^s\boldsymbol{u}^h = \boldsymbol{B}\boldsymbol{d}, \tag{28}$$

$$\nabla\cdot\boldsymbol{u}^h = \boldsymbol{b}\boldsymbol{d}, \tag{29}$$

$$\nabla p^h = \boldsymbol{E}\boldsymbol{p}. \tag{30}$$

Introducing these discrete functions into the residual equations, and recognizing the arbitrary nature of the weights $\boldsymbol{c}$ and $\bar{\boldsymbol{c}}$, we arrive at an algebraic statement of the problem: find $(\boldsymbol{d},\boldsymbol{p})_{n+1}$ such that

$$\begin{pmatrix}\boldsymbol{R}_G\\ \boldsymbol{R}_H\end{pmatrix}_{n+1} = \begin{pmatrix}\boldsymbol{G}^{\mathrm{ext}} - \boldsymbol{G}^{\mathrm{int}}\\ \Delta t\boldsymbol{H}^{\mathrm{ext}} - \Delta t\boldsymbol{H}^{\mathrm{int}}\end{pmatrix}_{n+1} = \boldsymbol{0}, \tag{31}$$

where

$$\boldsymbol{G}^{\text{int}}_{n+1} = \int_\Omega \boldsymbol{B}^{\mathrm{T}}(\boldsymbol{\sigma}'_{n+1} - p^h_{n+1}\mathbf{1})\mathrm{d}\Omega, \tag{32}$$

$$\boldsymbol{G}^{\text{ext}}_{n+1} = \int_\Omega (\boldsymbol{N}^d)^{\mathrm{T}}\rho\boldsymbol{g}\mathrm{d}\Omega + \int_{\Gamma_t} (\boldsymbol{N}^d)^{\mathrm{T}}\bar{\boldsymbol{t}}_{n+1}\mathrm{d}\Gamma, \tag{33}$$

$$\boldsymbol{H}^{\text{int}}_{n+1} = \int_\Omega \left[-(\boldsymbol{N}^p)^{\mathrm{T}}\boldsymbol{b}(\boldsymbol{d}_{n+1} - \boldsymbol{d}_n) + \boldsymbol{E}^{\mathrm{T}}\bar{\boldsymbol{v}}^h_{n+\theta}\right]\mathrm{d}\Omega, \tag{34}$$

$$\boldsymbol{H}^{\text{ext}}_{n+1} = \int_{\Gamma_q} (\boldsymbol{N}^d)^{\mathrm{T}}\bar{q}_{n+\theta}\mathrm{d}\Gamma. \tag{35}$$

The incremental solution for the Newton–Raphson update at the $k+1$ iteration is determined as

$$\begin{bmatrix} \boldsymbol{K} & \boldsymbol{\Theta} \\ \boldsymbol{\Theta}^{\mathrm{T}} & (\theta\Delta t)\boldsymbol{\Phi} \end{bmatrix}_k \begin{pmatrix} \Delta\boldsymbol{d} \\ \Delta\boldsymbol{p} \end{pmatrix}_{(k+1)} = \begin{pmatrix} \boldsymbol{R}_G \\ \boldsymbol{R}_H \end{pmatrix}_k, \tag{36}$$

where

$$\boldsymbol{K}_k = \int_\Omega \boldsymbol{B}^{\mathrm{T}}\boldsymbol{C}_k\boldsymbol{B}^{\mathrm{T}}\mathrm{d}\Omega, \tag{37}$$

$$\boldsymbol{\Theta} = -\int_\Omega \boldsymbol{b}^{\mathrm{T}}\boldsymbol{N}^d\mathrm{d}\Omega, \tag{38}$$

$$\boldsymbol{\Phi} = -\frac{1}{\rho_{\mathrm{f}}g}\int_\Omega \boldsymbol{E}^{\mathrm{T}}\boldsymbol{K}\boldsymbol{E}\mathrm{d}\Omega. \tag{39}$$

Here, $\boldsymbol{C}_k$ is a matrix of elastoplastic tangential moduli (corresponding to the fourth-order tensor $\mathbb{C}_k$ defined earlier), and $\boldsymbol{K}$ is a matrix of permeability coefficients.

We observe that the previous formulation reduces to an even simpler one if we consider a linear-elastic constitutive equation with constant moduli,

$$\boldsymbol{\sigma}' = \mathbb{C}^e : \boldsymbol{\epsilon}. \tag{40}$$

In this case, the linearization of the governing equations is exact, and Newton's method will converge in a single iteration. The tangent matrix $\boldsymbol{C}_k$ can be replaced with a constant matrix $\boldsymbol{C}$, and several of the right hand side terms simplify. In Section 4 we instead consider a nonlinear description for the effective stress-strain relationship, based on a critical state plasticity model.

3. Stabilized formulation

The goal in this section is to develop a stabilized formulation that allows for the successful use of Q4P4 elements in coupled deformation-diffusion problems. We first begin with a few preliminary observations, and then present a stabilized formulation based on the Polynomial-Pressure-Projection technique.

Let us first examine the algebraic problem (36) in the undrained limit. In this case, the linear system reduces to the form

$$\begin{bmatrix} \boldsymbol{K} & \boldsymbol{\Theta} \\ \boldsymbol{\Theta}^{\mathrm{T}} & \mathbf{0} \end{bmatrix} \begin{pmatrix} \Delta\boldsymbol{d} \\ \Delta\boldsymbol{p} \end{pmatrix} = \begin{pmatrix} \boldsymbol{R}_G \\ \boldsymbol{R}_H \end{pmatrix}, \tag{41}$$

where a zero-block appears in the (2,2) position. Matrices with the same block structure arise in a variety of constrained problems in solid and fluid mechanics. Although (41) can be thought of as a single problem, it is helpful rather to think of it as a series of algebraic problems parameterized by the element diameter h. The goal is to ensure that the approximate solution converges to the exact solution at optimal convergence rates as $h \to 0$.

To do so, it is necessary for the spaces S^h_u and S^h_p chosen for the displacement and pressure interpolation to satisfy the discrete LBB condition [4],

$$\sup_{\boldsymbol{v}^h \in S^h_u} \frac{\int_\Omega q^h \nabla\cdot\boldsymbol{v}^h \mathrm{d}\Omega}{\|\boldsymbol{v}^h\|_1} \geqslant C\|q^h\|_0 \quad \forall q^h \in S^h_p, \tag{42}$$

with $C > 0$ independent of h. Unfortunately, the spaces S^h_u and S^h_p associated with linear-pressure/linear-displacement interpolations do not satisfy this condition and lead to unstable approximations. In [24], however, Bochev et al. demonstrated that this pair does satisfy a weaker condition. Consider a projection operator $\Pi : L_2(\Omega) \to R_0$, where R_0 is the space of piecewise constants. The authors showed that the discrete spaces S^h_u and S^h_p satisfy

$$\sup_{\boldsymbol{v}^h \in S^h_u} \frac{\int_\Omega q^h \nabla\cdot\boldsymbol{v}^h \mathrm{d}\Omega}{\|\boldsymbol{v}^h\|_1} \geqslant C_1\|q^h\|_0 - C_2\|q^h - \Pi q^h\|_0 \quad \forall q^h \in S^h_p, \tag{43}$$

with $C_1 > 0$ and $C_2 > 0$ independent of h. Comparing this result with the discrete LBB condition, we see that the term $C_2\|q^h - \Pi q^h\|_0$ quantifies the inherent deficiency in the Q4P4 pair. The stabilization methodology is therefore to add stabilizing terms to the variational equations to penalize this deficiency. Schemes for the Stokes equations and Darcy equations can be found in [13,25]. We now take the same approach for the coupled deformation-diffusion problems under consideration.

We first need to define a projection operator with a suitable range – that of piecewise constants. Therefore, let

$$\Pi p^h|_{\Omega^e} = \frac{1}{V^e}\int_{\Omega^e} p^h \mathrm{d}\Omega. \tag{44}$$

Here, V^e is the volume of the element. The value of the projected field within each element is simply equal to the element average of p^h. We then modify the discrete variational equation for the balance of mass, $\mathscr{H}^h = 0$, to include an additional term,

$$\mathscr{H}^h - \mathscr{H}^{\text{stab}} = 0, \quad \mathscr{H}^{\text{stab}} = \int_\Omega \frac{\tau}{2G}(\psi^h - \Pi\psi^h)\overline{(\dot{p^h} - \Pi\dot{p^h})}\mathrm{d}\Omega. \tag{45}$$

The time-discrete version is

$$\begin{aligned} &\mathscr{H}^h_{n+1} - \mathscr{H}^{\text{stab}}_{n+1} = 0, \\ &\mathscr{H}^{\text{stab}}_{n+1} = \int_\Omega \frac{\tau}{2G_{n+\theta}\Delta t}(\psi^h - \Pi\psi^h)(p^h_{n+1} - \Pi p^h_{n+1} - p^h_n + \Pi p^h_n)\mathrm{d}\Omega. \end{aligned} \tag{46}$$

Here, G is the shear modulus and $\tau > 0$ is a constant multiplier. Typically this parameter is $\mathscr{O}(1)$, but it can be used to "tune" the level of stabilization. In the numerical examples we provide further discussion on this point. Note also that in equation (46) the shear modulus appears as a coefficient on the stabilizing term. In many hyperelastic and elastoplastic models, including those examined in this work, the shear modulus is a function of the current state of stress and will therefore evolve with the configuration. To be fully consistent in such cases, we evaluate

$$G_{n+\theta} = \theta G_{n+1} + (1-\theta)G_n. \tag{47}$$

The linearization of the stabilizing term about an intermediate configuration $(\boldsymbol{u}_k, p_k)$ is taken as

$$\Delta\mathscr{H}^{\text{stab}}_k = \int_\Omega \frac{\tau}{2G_k\Delta t}(\psi_h - \Pi\psi_h)[\Delta p^h_k - \Pi(\Delta p^h_k)]\mathrm{d}\Omega. \tag{48}$$

We note that additional terms associated with the linearization of the coefficient $1/G_k$ have been omitted. Unless the modulus changes dramatically over an increment, these additional contributions are minor and can be ignored without losing quadratic convergence behavior in the global Newton iterations.

The additional quantities associated with the stabilization scheme can be readily assembled into the matrix problem using standard shape function information. Noting that $\Pi(\psi^h) = \Pi(\boldsymbol{N}^p\bar{\boldsymbol{c}}) = \Pi(\boldsymbol{N}^p)\bar{\boldsymbol{c}}$, the stabilized version of Eq. (36) becomes

$$\left\{ \begin{bmatrix} \boldsymbol{K} & \boldsymbol{\Theta} \\ \boldsymbol{\Theta}^{\mathrm{T}} & (\theta\Delta t)\boldsymbol{\Phi} \end{bmatrix}_k - \begin{bmatrix} \mathbf{0} & \mathbf{0} \\ \mathbf{0} & \boldsymbol{S} \end{bmatrix}_k \right\} \begin{pmatrix} \Delta\boldsymbol{d} \\ \Delta\boldsymbol{p} \end{pmatrix}_{(k+1)} = \begin{pmatrix} \boldsymbol{R}_G \\ \boldsymbol{R}_H \end{pmatrix}_k + \begin{pmatrix} \mathbf{0} \\ \boldsymbol{H}^{\text{stab}}_{n+1} \end{pmatrix}_k, \tag{49}$$

where the two stabilizing terms are given by

$$\boldsymbol{H}^{\text{stab}}_{n+1} = \int_\Omega \frac{\tau}{2G_{n+\theta}} [\boldsymbol{N}^p - \Pi(\boldsymbol{N}^p)][p^h_{n+1} - \Pi p^h_{n+1} - p^h_n + \Pi p^h_n] \mathrm{d}\Omega, \quad (50)$$

$$\boldsymbol{S} = \int_\Omega \frac{\tau}{2G_{n+\theta}} [\boldsymbol{N}^p - \Pi(\boldsymbol{N}^p)][\boldsymbol{N}^p - \Pi(\boldsymbol{N}^p)] \mathrm{d}\Omega. \quad (51)$$

We see that the result of the scheme is to introduce a stabilizing sub-matrix into the (2,2) position, eliminating the zero-block that would otherwise appear in the incompressible case. Because the stabilization is based on the original shape functions, however, the sparsity pattern of this block remains unchanged and no fill-in occurs. Also note that modifications are only made to the pressure-pressure coupling block – the other sub-matrices remain unchanged. This is a key contrast with stabilization schemes based on adding residual equations to the variational form, for example, [18–20], where other sub-matrices are modified as well. Finally, unlike subgrid scale methods, the stabilization does not require additional basis functions or element level condensation.

4. Constitutive theory for slip weakening and shear-induced compaction

In this section we describe a constitutive theory for modeling the mechanical deformation behavior of the fault gouge material as well as the surrounding rock for a typical fault zone. Our assumption is that fluids are present in the fault zone and that they could play a major role in the weakening of the fault as it slips. We first describe the relevant background on the expected mechanisms in a fault zone, then elucidate the details of the constitutive model that is eventually used with the stabilized formulation. For simplicity we restrict the discussions of this section to isothermal deformation.

4.1. Background

Gouge is the name given to the highly damaged granular material representing the core of a fault that is the product of wear as sliding takes place [36]. Friction is a very important factor in the brittle behavior of rocks [37]. The coefficient of friction is known to depend on slip speed [38] and on a state variable reflecting the maturity of contact [39]. Healing increases the value of the coefficient of friction when the fault is stationary. When the stresses reach a certain critical value, however, the fault could undergo slip instability, causing a reduction in the value of the coefficient of friction. The process is called slip weakening, and during this process the shear stress τ_f on the fault can be written for a purely frictional fault as

$$\tau_\mathrm{f} = -\mu\sigma'_\mathrm{f} = f(\sigma'_\mathrm{f}, \Delta), \quad (52)$$

where μ is the coefficient of friction, σ'_f is the effective normal stress on the fault (negative for compression), and Δ is a measure of slip. The function $f(\sigma'_\mathrm{f}, \Delta)$ implies that when σ'_f is constant the coefficient of friction μ depends on slip Δ. The same function, however, could also be taken to mean that during slip weakening the normal stress σ'_f itself could also vary with slip. The latter possibility is shown schematically in Fig. 2 [40]: when the fault gouge undergoes shear-induced compaction (dilation) the pore pressure could increase (decrease), resulting in a reduction (increase) of $-\sigma'_\mathrm{f}$. Of course, these processes are linked to the coupled theory and could be influenced by the stabilized formulation.

The mechanism of interest is that of shear-induced compaction, and in order to model this process we employ a critical state plasticity model based on the Modified Cam-Clay (MCC) yield surface [41]. The plasticity model provides a compression cap that is essential for the simulation of plastic compaction. The constitutive framework can also capture several other features commonly observed in the behavior of soils and porous rocks – including pressure sensitivity, hardening response with plastic volumetric compaction, softening response with plastic dilation, and the possibility of isochoric plastic shear. As the focus of this paper is not on the constitutive model itself, however, we only briefly review the salient features and highlight those that are relevant for simulating the key mechanisms in a fault zone. A complete description, as well as the extension to finite deformations, has been presented by Borja et al. in [42] and companion papers.

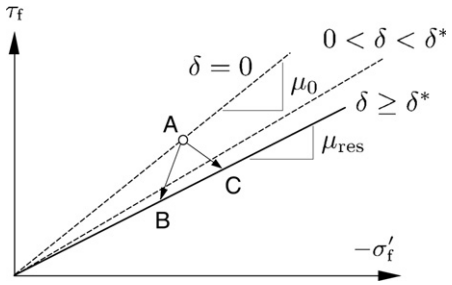

Fig. 2. Slip weakening of a frictional fault. During slip instability coefficient of friction decreases from initial value μ_0 when slip $\Delta = 0$ to residual value μ_res when slip $\Delta \geqslant \Delta^*$. AB = slip weakening with plastic compaction and pore pressure increase; AC = slip weakening with plastic dilation and pore pressure decrease (concept adapted from Wong [40]).

4.2. Hyperelastic response

We define mean normal stress p' and deviatoric stress q by

$$p' = \frac{1}{3}\mathrm{tr}(\boldsymbol{\sigma}'), \quad q = \sqrt{\frac{2}{3}}\|\boldsymbol{s}\|, \quad \boldsymbol{s} = \boldsymbol{\sigma}' - p'\boldsymbol{1}. \quad (53)$$

Using classical elastoplastic theory, the response inside a yield surface is governed by a hyperelastic model which produces pressure dependent elastic bulk and shear moduli. Hyperelasticity is derived from a stored energy density function of the form

$$\Psi(\epsilon^e_v, \epsilon^e_s) = -p_0\tilde{\kappa}\exp\Omega + \frac{3}{2}G\epsilon^{e2}_s, \quad \Omega = \frac{\epsilon^e_{v0} - \epsilon^e_v}{\tilde{\kappa}},$$
$$G = G_0 - \alpha p_0 \exp\Omega, \quad (54)$$

with volumetric and deviatoric strain invariants given by

$$\epsilon^e_v = \mathrm{tr}(\boldsymbol{\epsilon}^e), \quad \epsilon^e_s = \sqrt{\frac{2}{3}}\|\boldsymbol{\xi}^e\|, \quad \boldsymbol{\xi}^e = \boldsymbol{\epsilon}^e - \frac{1}{3}\epsilon^3_v\boldsymbol{1}. \quad (55)$$

The parameters of the model are the reference strain ϵ^e_{v0} and reference pressure p_0 of the elastic compression curve, the elastic compressibility index $\tilde{\kappa}$, and two parameters α and G_0 controlling the behavior of the shear modulus. Choosing $\alpha = 0$ leads to a constant elastic shear modulus $G = G_0$, while choosing $\alpha > 0$ produces a pressure-dependent modulus [43].

The effective stress $\boldsymbol{\sigma}'$ is determined as

$$\boldsymbol{\sigma}' = \frac{\partial\Psi}{\partial\boldsymbol{\epsilon}^e} = \frac{\partial\Psi}{\partial\epsilon^e_v}\frac{\partial\epsilon^e_v}{\partial\boldsymbol{\epsilon}^e} + \frac{\partial\Psi}{\partial\epsilon^e_s}\frac{\partial\epsilon^e_s}{\partial\boldsymbol{\epsilon}^e}. \quad (56)$$

Using the relationships

$$\frac{\partial\epsilon^e_v}{\partial\boldsymbol{\epsilon}^e} = \boldsymbol{1}, \quad \frac{\partial\epsilon^e_s}{\partial\boldsymbol{\epsilon}^e} = \sqrt{\frac{2}{3}}\hat{\boldsymbol{n}}, \quad \hat{\boldsymbol{n}} = \boldsymbol{\xi}^e/\|\boldsymbol{\xi}^e\|, \quad (57)$$

leads to the equivalent form

$$\boldsymbol{\sigma}' = p'\boldsymbol{1} + \sqrt{\frac{2}{3}}q\hat{\boldsymbol{n}}, \quad (58)$$

where p' and q can be derived from the elastic energy function as

$$p' = \frac{\partial \Psi}{\partial \epsilon^e} = p_0 \left[1 + \frac{3\alpha}{2\tilde{\kappa}} (\epsilon_s^e)^2 \right] \exp \Omega, \tag{59}$$

$$q = \frac{\partial \Psi}{\partial \epsilon^e} = 3(G_0 - \alpha p_0 \exp \Omega) \epsilon_s^e. \tag{60}$$

4.3. Plastic response

The elastic region is bounded by a two-invariant yield surface,

$$F = \frac{q^2}{M^2} + p'(p' - p'_c) = 0 \tag{61}$$

where $p'_c < 0$ is a plastic internal variable determining the size of the yield surface, and is known as the preconsolidation pressure. The material parameter $M > 0$ determines the slope of the critical state line (CSL), and is related to the continuum friction angle at critical state, ϕ_{cs} via [41]

$$M = \frac{6 \sin \phi_{cs}}{3 - \sin \phi_{cs}}. \tag{62}$$

The yield surface plots as a semi-ellipse on the p'–q plane. Inasmuch as we view the fault gouge as a continuum, slip weakening may now be viewed as a decrease in the value of M (or ϕ_{cs}) with shear strain Δ/h, where Δ is the relative slip of the two faces of the gouge separated by a thickness h.

We now examine the plastic behavior of the constitutive model. The model assumes an associative flow rule,

$$\dot{\epsilon} = \dot{\varphi} \frac{\partial F}{\partial \boldsymbol{\sigma}'} = \dot{\varphi} \left(\frac{1}{3} \frac{\partial F}{\partial p'} \mathbf{1} + \sqrt{\frac{3}{2}} \frac{\partial F}{\partial q} \hat{\boldsymbol{n}} \right),$$

$$\frac{\partial F}{\partial p'} = 2p' - p'_c, \qquad \frac{\partial F}{\partial q} = \frac{2q}{M^2}. \tag{63}$$

The condition for isochoric deformation is $\partial F / \partial p' = 0$, or $p' = p'_c/2$. This corresponds to a stress state at the peak of the ellipse, and separates two regions of the yield surface – one corresponding to plastic compaction and the other to plastic dilation. In the current work we do not consider the effect of non-associativity on the plastic response. There is sufficient experimental evidence supporting the associative flow rule for critical state models dating as far back as when Roscoe and Burland [41] first proposed the model. In the current case, the effect of non-associativity would be to reduce the plastic compaction for a given deviatoric plastic strain (the plastic flow direction is more deviatoric), thereby reducing the magnitude of pore pressure increase for the same plastic deviatoric strain. If non-associative effects are deemed important, however, we note that the current model is actually a subclass of a more general non-associative model developed by Borja in [44].

Hardening (or softening) is introduced through the parameter p'_c. Let e be the void ratio of the porous material, and define the specific volume as $v = (1 + e)$. It is commonly observed that a bilogarithmic relationship exists between the specific volume and the preconsolidation pressure; that is, in isotropic compression tests there is a linear relationship between $\ln(v)$ and $\ln(-p'_c)$, with the slope of this line represented by the compressibility index $\tilde{\lambda}$. Alternatively, one often sees experimental data plotted as e vs. $\ln(-p'_c)$. For an extensive comparison of these relationships, see [45,46]. The hardening law for the current model then takes the form,

$$\dot{p}'_c = \left(\frac{\mathrm{tr} \dot{\epsilon}^p}{\tilde{\lambda} - \tilde{\kappa}} \right) p'_c. \tag{64}$$

For illustration purposes, Fig. 3 compares the current constitutive model with fixed-ring oedometer tests by McKiernan and Saffer [47] on sediments extracted near the deformation front of the Costa Rica subduction zone.

We have omitted the details of the numerical implementation of the material subroutine, as an extensive presentation is already available in the literature. We note, however, that one difficulty in the implementation is that the elastic bulk and shear moduli are stress-dependent. This introduces considerable challenge for a classical return-mapping algorithm in stress space, since the predictor and corrector stresses are related to the elastic and plastic strains in a nonlinear fashion. Instead, we implement the model with a return-mapping algorithm in elastic strain space. This approach preserves the classical predictor-corrector operator split, and readily allows for the construction of consistent algorithmic tangent operators. Again, the interested reader is urged to consult [42] for further details.

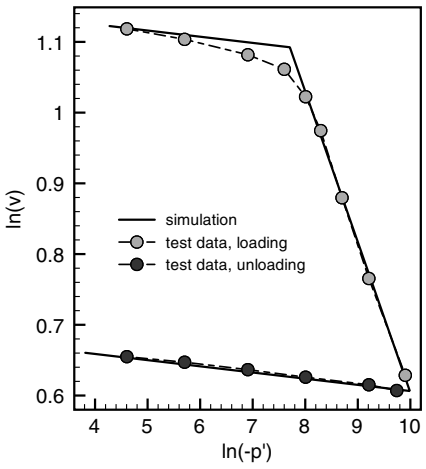

Fig. 3. Comparison of the current constitutive model with fixed-ring oedometer tests by McKiernan and Saffer [47] on subduction zone sediments.

5. Numerical examples

We now present three numerical examples to test the performance of the stabilization technique. Two of the examples are drawn from geotechnical applications, while the last is devoted to modeling an idealized fault zone. The examples were implemented using the `deal.II` Finite Element Library – a collaborative, open-source project focused on developing a toolbox of common algorithms and data structures for use in object-oriented finite element codes [48]. All linear systems were solved using the `UMFPACK` unsymmetric multifrontal direct solver [49].

5.1. Terzaghi's problem

Few analytical solutions exist for coupled consolidation problems. One classic example for which such a solution does exist is Terzaghi's one-dimensional problem. The domain consists of a linear-elastic soil mass of height h and infinite extent (Fig. 4). The

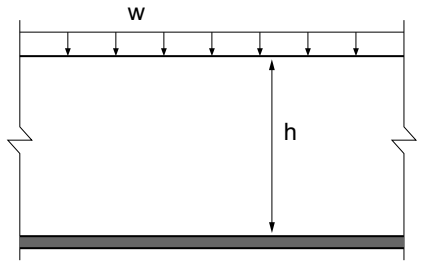

Fig. 4. Geometry and loading profile for Terzaghi's problem.

lower boundary is rigidly fixed and impermeable, while the upper boundary is fully drained ($p = 0$). At the initial time, a distributed load w is suddenly applied, leading to an instantaneous rise in pore pressures, after which these pressures dissipate. The mesh used for the problem consists of a single column of quadrilateral elements, which are restrained in the horizontal direction but can displace vertically. The linear elastic behavior of the soil is characterized by the two Lamé parameters, with $\lambda = 0$ and $G = 0.5$ kPa. The other model parameters are $\gamma_s = 0$, $\gamma_f = 10.0\ \text{kN/m}^3$, $\Delta t = 1.0$ s, and $k = 10^{-5}$ m/s. The stabilization coefficient is simply $\tau = 1$.

Fig. 5 presents the pressure profiles after the initial step, with the exact solution indicated by the thin dashed line. The pore pressures throughout the domain are equal to the overburden stress, except for in a thin layer near the drainage boundary. The unstable Q4P4 element, however, predicts wild oscillations in the pressure field. In contrast, the stable Q9P4 and stabilized Q4P4 perform well. The sharp gradient in the pressure profile near the drainage boundary poses a challenge for standard finite element methods, however, and lead to some minor oscillations even in the stable elements. Nevertheless, these oscillations do not propagate to the rest of the domain, and the performance of the two stable elements is far superior to the Q4P4.

We note that with progressing time, the initial errors in the pressure field for the Q4P4 element slowly dissipate. A careful study of this effect can be found in [34]. Clearly, however, the behavior at early times is unacceptable.

5.2. Strip footing

The next test case is a plane-strain strip footing. The geometry and loading profile are indicated in Fig. 6. From symmetry considerations only half of the domain is modeled. The soil behavior is described by the critical state plasticity model of Section 4, with the following model parameters: $\tilde{\kappa} = 0.05$, $\tilde{\lambda} = 0.20$, $\alpha = 0$, $G_0 = 200$ kPa, $M = 1.0$, $\gamma_s = 20\ \text{kN/m}^3$, and $\gamma_f = 10\ \text{kN/m}^3$. The initial time step is $\Delta t = 1$ day, after which increasingly large steps are taken using the recurrence relation $\Delta t_{n+1} = 1.2\Delta t_n$. Again, the stabilization coefficient is simply $\tau = 1$.

Since the model does not allow for a stress-free state, special care must be taken to establish initial conditions. We assume that the soil formation is normally consolidated throughout, with initial stresses due to gravity loads assigned based on a prior elastic analysis. A small surface load of 1 kPa, representing overburden pressures, is also applied. For a more complete discussion on methods for establishing initial geostatic conditions in elastoplastic problems, see [50].

In this example, we analyze two cases. In the first the permeability has an extremely low value of $k = 10^{-9}$ m/day, leading to locally undrained conditions within the time scale considered. The second case has a much higher permeability value of $k = 0.01$ m/day. In both cases, the strip load indicated in Fig. 6 is applied at a rate of 1 kPa/day over five days. Once a peak load of 5 kPa is reached, it is held constant for the remainder of the simulation. In the high-permeability simulation, the surface to the right of the footing is treated as a drainage boundary ($p = 0$). In the low permeability simulation, however, this surface boundary is treated as undrained. In this situation, the length scale over which drainage can take place is so short that the current coarse mesh is insufficient to resolve a meaningful boundary layer.

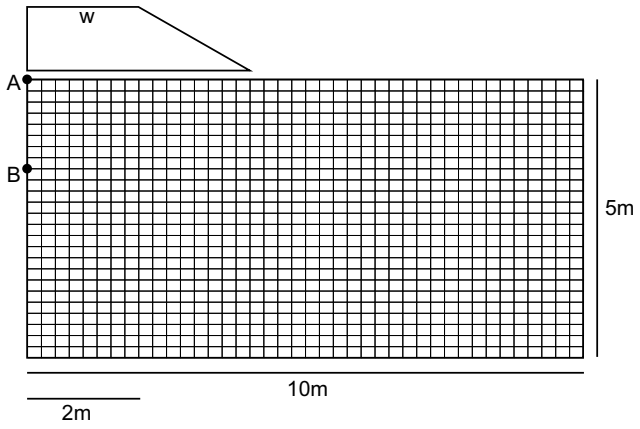

Fig. 6. Mesh and loading profile used for the elastoplastic footing example.

Fig. 7 shows contours of constant pressure at $t = 5$ days for the low-permeability simulation. Again, we observe oscillations in the Q4P4 element, while the Q9P4 and Q4P4s produce smooth solutions. The two stable solutions compare well with each other. Some differences, however, can be observed in the contours near the upper boundary. Fig. 8 compares the time-histories of pressure and displacement for the undrained case at two points in the domain (points A and B). Since the medium is locally undrained, we expect that once the peak load has been applied, pressures and displacements should remain constant for the remainder of the simulation. The Q9P4 and Q4P4s elements reproduce the expected behavior. Furthermore, the maximum difference in the curves for these two elements is less than 0.1%.

In contrast, the unstable Q4P4 grossly underpredicts the pressure at the end of the loading sequence. Afterward, the pressure appears to oscillate around the reference Q9P4 solution. Ultimately the erroneous pressures dissipate with time and the quality of the unstable Q4P4 solution improves. We see, however, that these ini-

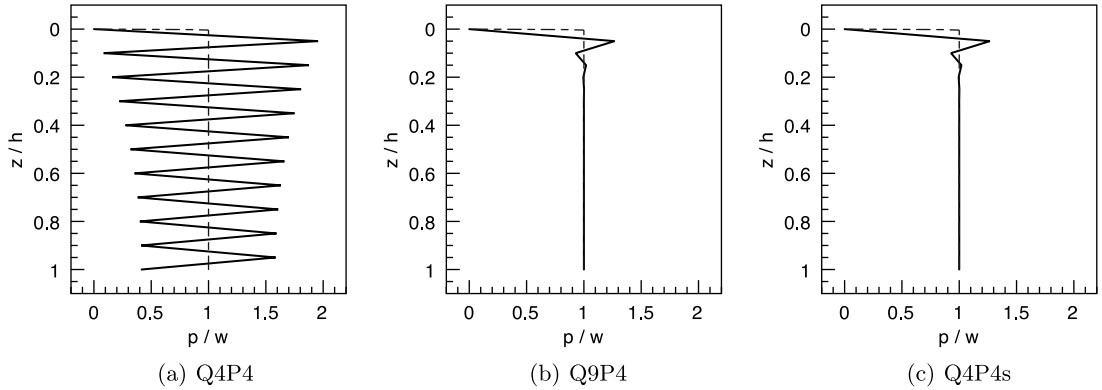

Fig. 5. Pressure profiles at the end of the first time-step for different element types applied to Terzaghi's consolidation problem, with $k = 10^{-5}$ m/s. The exact solutions are indicated by the dashed lines.

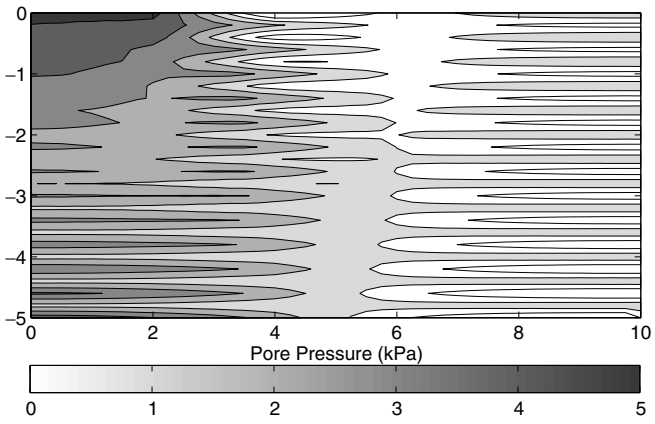

(a) Q4P4

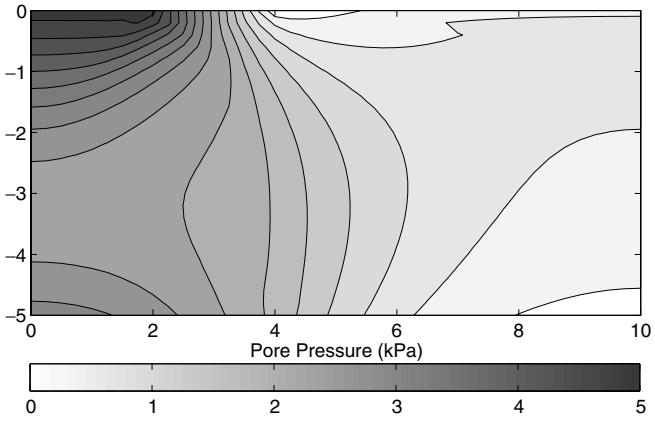

(b) Q9P4

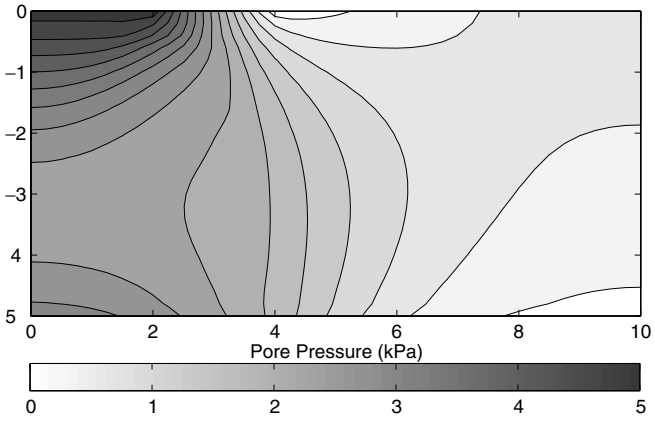

(c) Q4P4s

Fig. 7. Contours of constant pore pressure for the elastoplastic footing problem at $t = 5$ days for the $k = 10^{-9}$ m/day case.

tial errors persist for quite a while, and do not even capture the qualitative behavior of the true solution. The displacement histories for all three elements (even the unstable Q4P4) match closely, as the spurious pressure modes are uncoupled from the displacements.

Turning now to the high-permeability case (Fig. 9), no instabilities are observed, and all three elements perform well. We note that after the peak load has been applied, the pressure rises slightly before beginning to dissipate. This initial rise in pore pressures is the well-known Mandel-Cryer effect [51], a signature of the

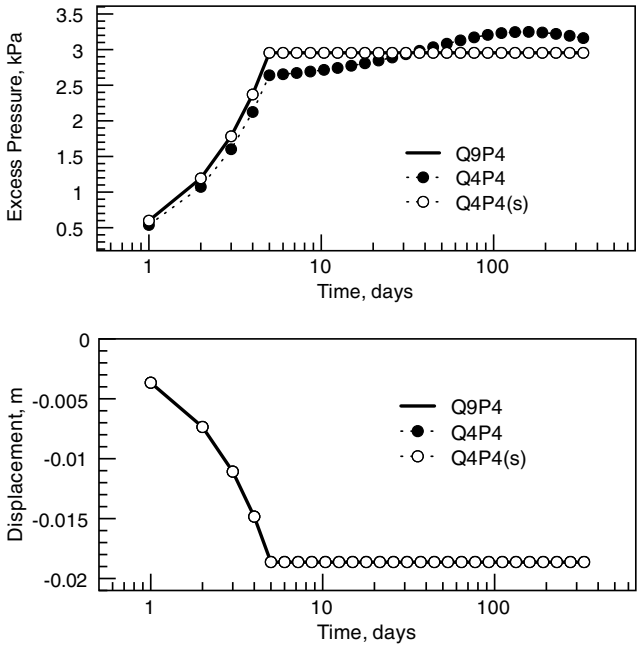

Fig. 8. Time-histories for the elastoplastic footing example, locally undrained case with $k = 10^{-9}$ m/day. Displacement is measured at point A, and pressure at point B.

coupled solid/fluid flow problem that cannot be captured by uncoupled or loosely coupled solution strategies.

In the high-permeability case, it appears then that there is no advantage to employing a stabilized formulation. Indeed, the unstable Q4P4 is often used in practice without stabilization because good results can be achieved in such cases. The reason we have presented this example, however, is to emphasize that the stabilization scheme causes no unusual behavior in the high-permeability limit, and can therefore be used across the complete range from compressible to incompressible. As the method introduces trivial additional computational expense and can be added

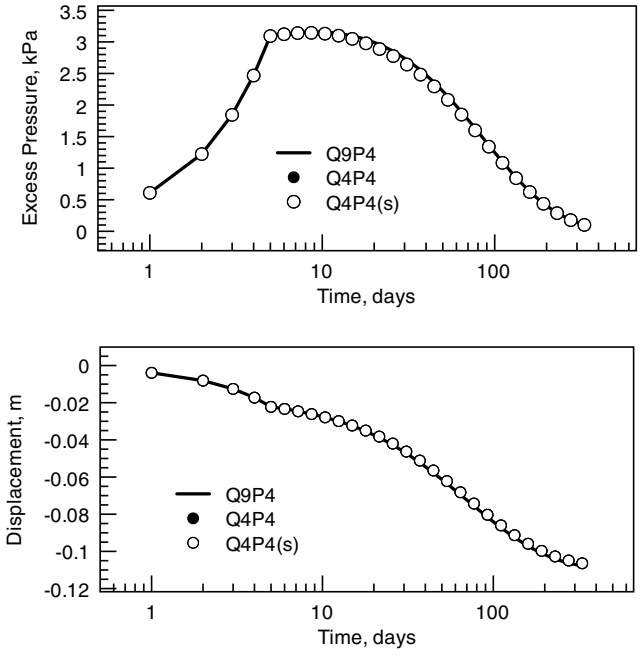

Fig. 9. Time-histories for the elastoplastic footing example, high-permeability case with $k = 0.01$ m/day.

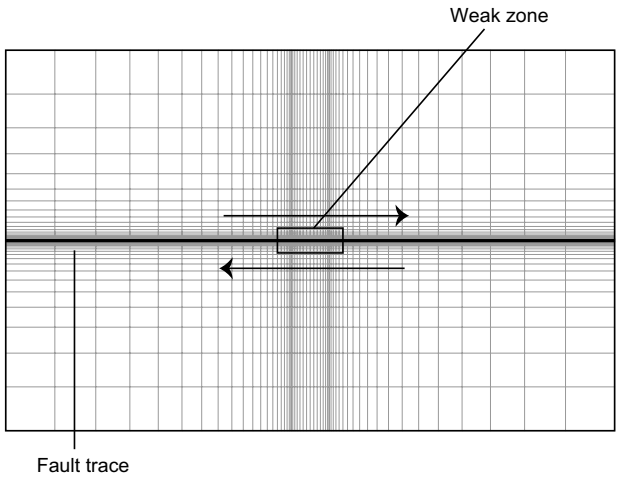

Fig. 10. Mesh used for the fault zone analysis. The mesh is refined around the fault trace and the slip weakening zone. The domain is 40 m×25 m and the weak zone is 2.5 m in length. The arrows indicate the direction of slip.

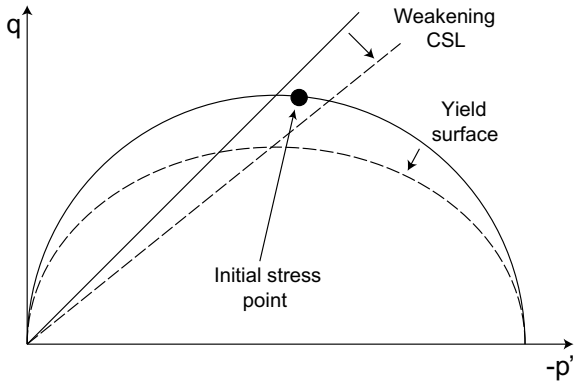

Fig. 11. Schematic diagram illustrating the weakening process.

with minimal coding effort, we argue that is is practical to use the proposed scheme at all times, instead of having a specialized formulation that is only used when incompressible behavior appears.

5.3. Weakening of a fault segment

Our final example is of an idealized fault zone. The mesh used for the analysis is indicated in Fig. 10. The geometry consists of a thin but finite width fault running horizontally through the surrounding host rock. This surrounding formation is modeled as hyperelastic, while a critical state plasticity model is used for the fault gouge itself. The model parameters are as follows: $\tilde{\kappa} = 0.03$, $\tilde{\lambda} = 0.18$, $\alpha = 0$, $M = 1.2$, $\gamma_s = 20\text{kN/m}^3$, $\gamma_f = 10\ \text{kN/m}^3$, $k = 10^{-10}$ m/day. The shear modulus for the host rock is $G_0 = 5 \times 10^5$ kPa, while a weaker modulus of 5×10^3 is used for the fault gouge. The initial time step is $\Delta t = 1$ day, after which increasingly large steps are taken using the recurrence relation $\Delta t_{n+1} = 1.2\Delta t_n$. The modeled domain is 40 m×25 m, with a 0.2 m-thick fault.

To simulate faulting behavior, we assume that the domain is in a state of high shear near the CSL and slightly on the compression cap of the yield surface, but is in static equilibrium. At some initial time, however, a small portion of the fault (2.5 m) weakens due to a small amount of slip – induced, for example, by material instability [52]. As a result, the domain is no longer in equilibrium and fur-

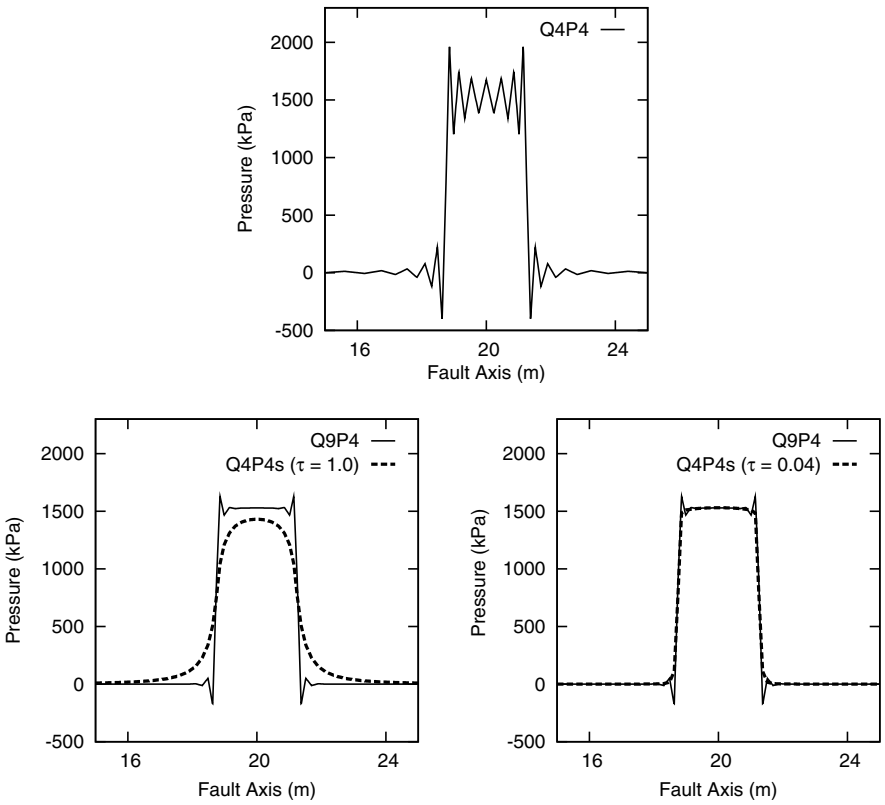

Fig. 12. Pressure profile along the fault axis for each of the three elements after one time-step. In the case of the Q4P4s element, solutions are computed using two values of the stabilization parameter τ.

ther slip is nucleated on the weak zone – which then propagates to the rest of the fault trace. Since the fault is assumed to be saturated and the initial stress points are located on the compression cap of the yield surface, we observe a sudden rise in pore-pressures due to shear-induced compaction [53].

Again, the initial state of stress is crucial for the model. We assume that the fault has undergone significant plastic shear in the past, and thus the material in the fault should be close to critical state. This idea is indicated schematically in Fig. 11, which illustrates the initial stress point and yield surface for the material within the fault. To simulate the weakening event along the central portion, the slope of the CSL is suddenly lowered. This causes the yield surface to flatten (assuming p'_c remains fixed during slip weakening), and initiates plastic shear as well as a small amount of plastic compaction. The time-frame over which this deformation occurs, however, is controlled by the permeability of the formation.

Fig. 12 plots the trace of the pore-pressure along the axis of the fault after the initial time-step. We see that the slip event leads to a sharp rise in pressure within the weakened zone. The Q4P4 element produces spurious pressures, as expected, but the Q9P4 also displays slight oscillations as well. This is to be expected, since the pressure profile is almost a step-function, and even our refined

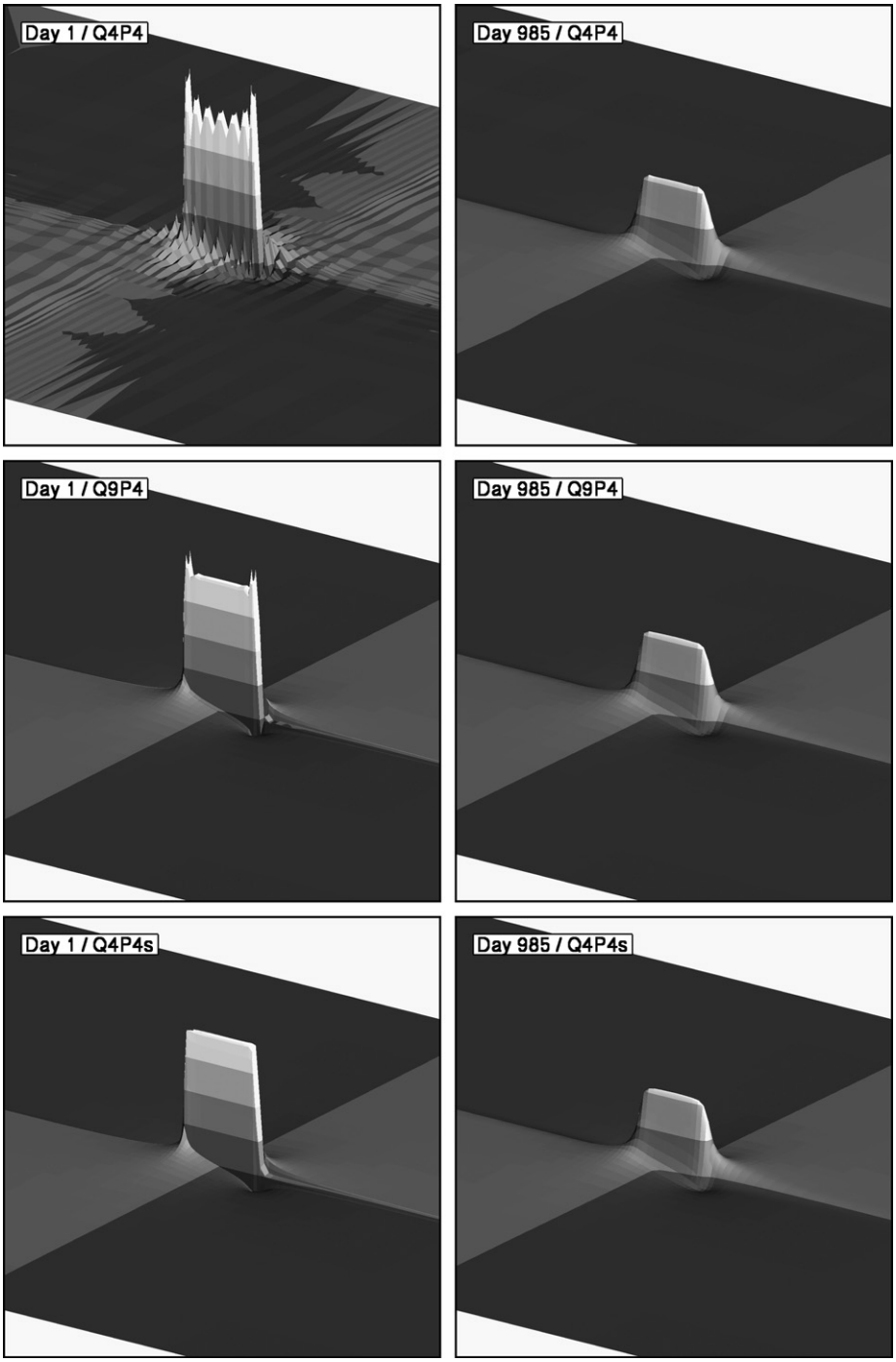

Fig. 13. 3D surfaces showing the pressure profile around the slip zone for each of the three element types. The left column is the pressure after 1 day, and the right is after 985 days.

mesh may be insufficient to capture this behavior. Nevertheless, this simulation provides a good illustration of a potential shortcoming of the stabilization scheme. Fig. 12 compares the predicted profile for the stabilized Q4P4s to the stable Q9P4 using two values of the stabilization parameter τ. In both cases we find smooth solutions, but using $\tau = 1$ (as we have for the other examples in this paper) leads to an overly diffuse profile. Examining Eq. (46), it appears that the gradients in the solution are so large that the stabilization severely over-relaxes the continuity equation and leads to a poor solution. Fortunately, the situation can be remedied by decreasing the magnitude of the stabilization coefficient τ for the elements within the fault zone. Choosing $\tau = 0.04$, a sharp pressure profile is recovered, with peak values in agreement with the Q9P4 solution.

This example suggests that in practice the analyst should be sure to examine the sensitivity of the solution to the stabilization

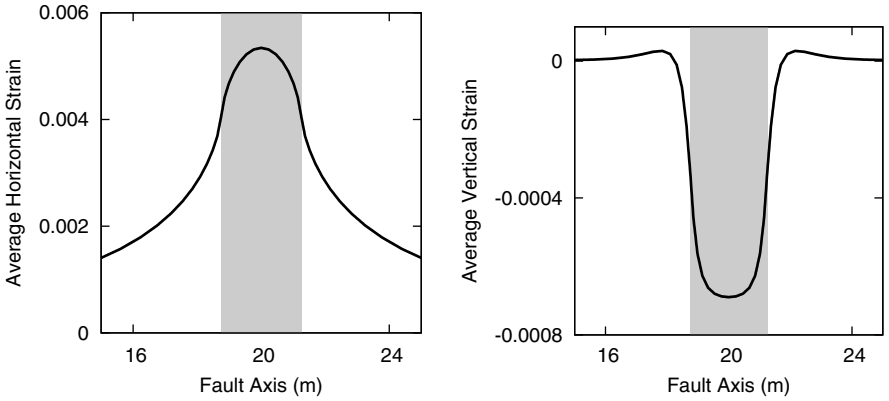

Fig. 14. Horizontal and vertical strains along the fault trace, averaged over the fault thickness, at $t = 985$ days. The gray bars indicate the width of the weak zone where slip was triggered.

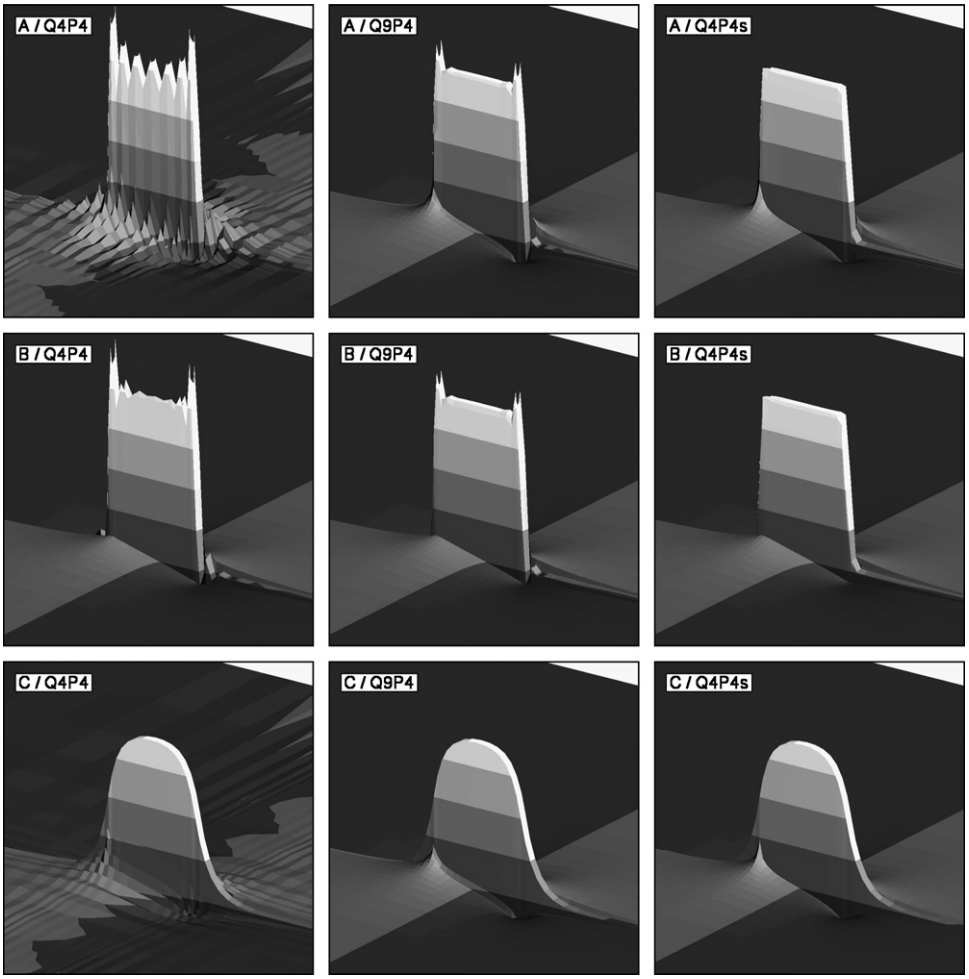

Fig. 15. Comparison of the predicted pressure profiles for the three permeability cases, A-C.

parameter τ. Of course, this is good advice with respect to any simulation parameter. The current example represents an extreme case, however, and for smooth solutions choosing a good τ value should be relatively straightforward.

To examine the behavior of the fluid pressures in the surrounding host rock, Fig. 13 presents surface plots of the pore pressure in the near field around the weakened zone at $t = 1$ day and at $t = 985$ days. In the case of the unstable element, spurious modes are visible throughout the domain. As time passes, however, these modes are slowly damped until eventually a smooth solution is recovered. The presence of relatively large pressures even after 985 days indicates that, in such a low-permeability formation, the dissipation of excess pore-pressures can take several years until a new equilibrium configuration is achieved.

The kinematic behavior of the fault is presented in Fig. 14, which plots horizontal and vertical strains along the fault trace. These strains are an average over the fault thickness, computed as the relative displacement between the upper and lower edge of the fault divided by the fault thickness. All three elements produce good displacement solutions, with essentially identical results, so separate figures are omitted. Interestingly, though slip was initiated on a relatively short segment, a significant portion of the surrounding fault has been activated as well. Furthermore, vertical strains signify a significant level of shear induced compaction within the weakened zone, as expected.

Before concluding this section, we present a brief parametric study. We wished to study the robustness of the stabilization scheme in the presence of sharp discontinuities in material coefficients. The previously presented fault analysis has already somewhat addressed this issue, as the shear modulus for the fault material was taken as 100 times weaker than the surrounding host rock. We now consider the behavior of the scheme when the permeability varies by several orders of magnitude between host rock and fault gouge. Capturing this behavior also has practical relevance to field observations of fault behavior, where the permeability of the material within the fault commonly differs significantly from the surrounding rock as a result of the evolution process, and may be either more or less permeable.

The study consists of three cases. Case A is the previously examined base case, where the hydraulic conductivity in the fault, k_{in}, is the same as the conductivity outside the fault, k_{out}, with $k_{\text{in}} = k_{\text{out}} = 1 \times 10^{-10}$ m/day. For Case B, the permeability in the surrounding host rock is several orders of magnitude higher, such that $k_{\text{in}} = 1 \times 10^{-10}$ m/day and $k_{\text{out}} = 1 \times 10^{-6}$ m/day. Case C is the reverse, a highly permeable fault with $k_{\text{in}} = 1 \times 10^{-6}$ m/day and $k_{\text{out}} = 1 \times 10^{-10}$ m/day.

Fig. 15 presents the predicted pressure surfaces in the region around the slip zone for each of the three elements and each of the three test configurations. In all cases, we find that the stabilized formulation performs well, with no instability observed. Indeed, the presence of higher permeability regions introduces compressibility that tends to mitigate the appearance of oscillations in those regions, and the stabilization introduces no unusual behavior at the interface. Though not presented, we have examined a variety of other permeability configurations – in both higher and lower ratios – and found satisfactory results in all cases.

The stabilized formulation provides a convenient means of modeling compressible, nearly compressible, and incompressible behavior in the same domain. The key difficulty, however, that even the stabilized element cannot escape is that jumps in material coefficients may introduce large solution gradients across the interface, requiring severe mesh refinement if a continuous element is to be employed. The small oscillations observed with even the Q9P4 element are symptomatic of this effect. Indeed, depending on the time and length scales associated with the problem investigated, it may be inappropriate to enforce strict continuity of the pressure in such cases.

6. Closure

Stabilized methods can offer tremendous computational advantages over standard approaches. In particular, one can employ meshes with fewer degrees of freedom, fewer Gauss points, and simpler data structures. The additional stabilization terms can also improve the convergence properties of iterative solvers. These factors become crucial when considering large-scale, coupled, three-dimensional problems.

In this work we have proposed a stabilization scheme to allow for the use of Q4P4 elements, though the same scheme can also be applied to simplicial elements and three-dimensions. The method employed has several appealing features. It requires only a minor modification of standard finite element codes, and adds little additional computational cost to the assembly routines. All necessary computations can be performed at the element level using standard shape-function information, and no higher-order derivatives or stress-recovery techniques must be employed. It also leads to a symmetric modification of the system matrix, which is advantageous if the underlying problem is symmetric.

As the numerical examples have demonstrated, the stabilization scheme is robust and leads to high-quality solutions. In our opinion the key disadvantage is that the resulting solution may be overly diffusive in the presence of extremely sharp gradients, such as those encountered during the fault-zone analysis. As we have indicated, this is an extreme case and the effect can be controlled using the stabilization parameter τ.

Future work will include extending the stabilization scheme to other useful elements such as the Q4P0. Additional investigation should also be devoted to exploring the behavior of stabilization schemes near boundaries, as it is well known that many schemes have degraded accuracy in these regions [54]. More detailed studies of the interaction of the stabilization scheme with the time integration method would also be of interest.

The general conclusion, however, is that the computational advantages offered by stabilized methods are very appealing. This fact will prove useful as we look towards demanding, larger-scale models of fault zone behavior, especially those employing coupled microscale/macroscale simulation techniques [55].

Acknowledgements

We are grateful to the reviewers for their suggestions and expert reviews. This work is supported in part by the US Department of Energy Grant No. DE-FG02-03ER15454, and National Science Foundation Grant No. CMG-0417521 (Collaborations in Mathematical Geosciences). The first author acknowledges graduate fellowship support from The National Science Foundation and Stanford University's Graduate Fellowship Program.

References

[1] N.H. Sleep, M.L. Blanpied, Creep, compaction and the weak rheology of major faults, Nature 359 (6397) (1992) 687–692.
[2] J.L. Hardebeck, E. Hauksson, Role of fluids in faulting inferred from stress field signatures, Science 285 (5425) (1999) 236–239.
[3] P. Segall, J.R. Rice, Dilatancy, compaction, and slip instability of a fluid-infiltrated fault, J. Geophys. Res. 100 (B11) (1995) 22155–22172.
[4] F. Brezzi, A discourse on the stability conditions for mixed finite element formulations, Comput. Methods Appl. Mech. Engrg. 82 (1-3) (1990) 27–57.
[5] D.N. Arnold, Mixed finite element methods for elliptic problems, Comput. Methods Appl. Mech. Engrg. 82 (1990) 81–300.
[6] D.N. Arnold, F. Brezzi, M. Fortin, A stable finite element for the Stokes equations, Calcolo 21 (4) (1984) 337–344.

[7] B. Jha, R. Juanes, A locally conservative finite element framework for the simulation of coupled flow and reservoir geomechanics, Acta Geotech. 2 (3) (2007) 139–153.
[8] F. Brezzi, J. Pitkäranta, On the stabilization of finite element approximations of the Stokes problem, Eff. Solut. Ellip. Syst. (1984) 11–19.
[9] T.J.R. Hughes, L.P. Franca, M. Balestra, A new finite element formulation for computational fluid dynamics: V. Circumventing the Babuška-Brezzi condition: a stable Petrov-Galerkin formulation of the Stokes problem accommodating equal-order interpolations, Comput. Methods Appl. Mech. Engrg. 59 (1) (1986) 85–99.
[10] T.J.R. Hughes, G.R. Feijóo, L. Mazzei, J.B. Quincy, The variational multiscale method – a paradigm for computational mechanics, Comput. Methods Appl. Mech. Engrg. 166 (1-2) (1998) 3–24.
[11] J. Douglas, J. Wang, An absolutely stabilized finite element method for the Stokes problem, Math. Comput. 52 (186) (1989) 495–508.
[12] A. Masud, T.J.R. Hughes, A stabilized mixed finite element method for Darcy flow, Comput. Methods Appl. Mech. Engrg. 191 (39-40) (2002) 4341–4370.
[13] C.R. Dohrmann, P.B. Bochev, A stabilized finite element method for the Stokes problem based on polynomial pressure projections, Int. J. Numer. Methods Fluids 46 (2004) 183–201.
[14] E. Oñate, J. Rojek, R. Taylor, O. Zienkiewicz, Finite calculus formulation for incompressible solids using linear triangles and tetrahedra, Int. J. Numer. Methods Engrg. 59 (2004) 1473–1500.
[15] A. Masud, K. Xia, A stabilized mixed finite element method for nearly incompressible elasticity, J. Appl. Mech. 72 (2005) 711.
[16] A. Masud, K. Xia, A variational multiscale method for inelasticity: Application to superelasticity in shape memory alloys, Comput. Methods Appl. Mech. Engrg. 195 (33-36) (2006) 4512–4531.
[17] I. Romero, M. Bischoff, Incompatible bubbles: A non-conforming finite element formulation for linear elasticity, Comput. Methods Appl. Mech. Engrg. 196 (9-12) (2007) 1662–1672.
[18] J. Wan, Stabilized finite element methods for coupled geomechanics and multiphase flow. Ph.D. Thesis, Stanford University, 2002.
[19] A. Truty, A Galerkin/least-squares finite element formulation for consolidation, Int. J. Numer. Methods Engrg. 52 (2001) 763–786.
[20] A. Truty, T. Zimmermann, Stabilized mixed finite element formulations for materially nonlinear partially saturated two-phase media, Comput. Methods Appl. Mech. Engrg. 195 (2006) 1517–1546.
[21] M. Pastor, O.C. Zienkiewicz, T. Li, Stabilized finite elements with equal order of interpolation for soil dynamics problems, Arch. Comput. Methods Engrg. 6 (1) (1999) 3–33.
[22] M. Pastor, T. Li, X. Liu, O.C. Zienkiewicz, M. Quecedo, A fractional step algorithm allowing equal order of interpolation for coupled analysis of saturated soil problems, Mech. Cohes. Frict. Mater. 5 (7) (2000) 511–534.
[23] X. Li, X. Han, M. Pastor, An iterative stabilized fractional step algorithm for finite element analysis in saturated soil dynamics, Comput. Methods Appl. Mech. Engrg. 192 (35-36) (2003) 3845–3859.
[24] P.B. Bochev, C.R. Dohrmann, M.D. Gunzburger, Stabilization of low-order mixed finite elements for the Stokes equations, SIAM J. Numer. Anal. 44 (1) (2006) 82–101.
[25] P.B. Bochev, C.R. Dohrmann, A computational study of stabilized, low-order C^0 finite element approximations of Darcy equations, Comput. Mech. 38 (2006) 323–333.
[26] E. Burman, Pressure projection stabilizations for Galerkin approximations of Stokes' and Darcy's problem, Numer. Methods Partial Different. Equat. 24 (1) (2007) 127–143.
[27] M. Benzi, G.H. Golub, J. Liesen, Numerical solution of saddle point problems, Acta Numer. 14 (2005) 1–137.
[28] Y. Ben-Zion, J.R. Rice, Dynamic simulation of slip on a smooth fault in an elastic solid, J. Geophys. Res. 102 (1997) 17771–17784.
[29] R.I. Borja, C.D. Foster, Continuum mathematical modeling of slip weakening in geological systems, J. Geophys. Res. 112 (2007) B04301.
[30] Y. Ida, Cohesive force across the tip of a longitudinal shear crack and Griffith's specific surface energy, J. Geophys. Res. 77 (1972) 3796–3805.
[31] T.-F. Wong, Shear fracture energy of Westerly granite from post-failure behavior, J. Geophys. Res. 87 (1982) 990–1000.
[32] M.A. Biot, General theory of three-dimensional consolidation, J. Appl. Phys. 12 (2) (1941) 155–164.
[33] M.A. Biot, Theory of elasticity and consolidation for a porous anisotropic solid, J. Appl. Phys. 26 (2) (1955) 82–185.
[34] M.A. Murad, A.F.D. Loula, On stability and convergence of finite element approximations of Biot's consolidation problem, Int. J. Numer. Meth. Engrg. 37 (1994) 645–667.
[35] R.I. Borja, One-step and linear multistep methods for nonlinear consolidation, Comput. Methods Appl. Mech. Engrg. 85 (3) (1991) 239–272.
[36] M.S. Paterson, T.-F. Wong, Experimental Rock Deformation – The Brittle Field, second ed., Springer-Verlag, Berlin, Heidelberg, 2005.
[37] C.H. Scholz, The Mechanics of Earthquakes and Faulting, Cambridge Univ. Press, New York, 1990.
[38] J.H. Dieterich, Modeling of rock friction 1. Experimental results and constitutive equations, J. Geophys. Res. 84 (1979) 2161–2168.
[39] A.L. Ruina, Slip instability and state variable friction laws, J. Geophys. Res. 88 (1983) 10359–10370.
[40] T.-F. Wong, On the normal stress dependence of the shear fracture energy. in: S. Das, J. Boatwright, and C.H. Scholz (Eds.), Earthquake Source Mechanics, Geophys. Monogr. Ser., Vol. 37. Washington D.C., AGU., 1986, pp. 1–11.
[41] K.H. Roscoe, J.B. Burland, On the generalized stress–strain behaviour of 'wet' clay, Engrg. Plast. 3 (1968) 539–609.
[42] R.I. Borja, C. Tamagnini, Cam-Clay plasticity Part III: Extension of the inifinitesimal model to include finite strains, Comput. Methods Appl. Mech. Engrg. 155 (1998) 73–95.
[43] R.I. Borja, Coupling plasticity and energy-conserving elasticity models for clays, J. Geotech. Geoenviron. Engrg. ASCE 123 (10) (1999) 948.
[44] R.I. Borja, Cam-Clay plasticity. Part V: A mathematical framework for three-phase deformation and strain localization analyses of partially saturated porous media, Comput. Methods Appl. Mech. Engrg. 193 (48-51) (2004) 301–5338.
[45] R. Butterfield, A natural compression law for soils, Géotechnique 29 (1979) 468–480.
[46] K. Hasiguchi, On the linear relations of V-ln p and ln v-ln p for isotropic consolidation of soils, Int. J. Numer. Analyt. Methods Geomech. 19 (1995) 367–376.
[47] A.W. McKiernan and D.M. Saffer, Data report: Permeability and consolidation properties of subducting sediments off Costa Rica, ODP Leg 205. in: J.D. Morris, H.W. Villinger, and A. Klaus (Eds.), Proc. ODP, Sci. Results, vol. 205. 2006, pp. 1–24.
[48] W. Bangerth, R. Hartmann, G. Kanschat, deal.II – a general purpose object oriented finite element library, ACM Trans. Math. Software 33 (4) (2007) 27. Article 24.
[49] T.A. Davis, Algorithm 832: UMFPACK v4.3 – an unsymmetric-pattern multifrontal method, ACM Trans Math. Software 30 (2) (2004) 196–199.
[50] R.I. Borja, S.R. Lee, Cam-Clay plasticity, part I: Implicit integration of elastoplastic constitutive relations, Comput. Methods Appl. Mech. Engrg. 78 (1) (1990) 49–72.
[51] T.W. Lambe, R.V. Whitman, Soil Mechanics, Wiley, New York, 1968.
[52] R.I. Borja, Conditions for instabilities in collapsible solids including volume implosion and compaction banding, Acta Geotech. 1 (2) (2006) 107–122.
[53] R.I. Borja, Condition for liquefaction instability in fluid-saturated granular soils, Acta Geotech. 1 (4) (2006) 11–224.
[54] R. Becker, M. Braack, A finite element pressure gradient stabilization for the Stokes equations based on local projections, Calcolo 38 (2001) 173–199.
[55] J.A. White, R.I. Borja, J.T. Fredrich, Calculating the effective permeability of sandstone with multiscale lattice Boltzmann/finite element simulations, Acta Geotech. 1 (4) (2006) 195–209.